

Weak-Jamming Detection in IEEE 802.11 Networks: Techniques, Scenarios and Mobility

Martijn Hanegraaf^a, Savio Sciancalepore^{a,*}, Gabriele Oligeri^b

^aEindhoven University of Technology (TU/e), Eindhoven, Netherlands

^bHamad Bin Khalifa University (HBKU), College of Science and Engineering (CSE), Doha, Qatar

Abstract

State-of-the-art solutions detect jamming attacks *ex-post*, i.e., only when jamming has already disrupted the wireless communication link. In many scenarios, e.g., mobile networks or static deployments distributed over a large geographical area, it is often desired to detect jamming at the early stage, when it affects the communication link enough to be detected but not sufficiently to disrupt it (detection of *weak* jamming signals). Under such assumptions, devices can enhance situational awareness and promptly apply mitigation, e.g., moving away from the jammed area in mobile scenarios or changing communication frequency in static deployments, before jamming fully disrupts the communication link. Although some contributions recently demonstrated the feasibility of detecting low-power and weak jamming signals, they make simplistic assumptions far from real-world deployments. Given the current state of the art, no evidence exists that detection of weak jamming can be considered with real-world communication technologies.

In this paper, we provide and comprehensively analyze new general-purpose strategies for detecting weak jamming signals, compatible by design with one of the most relevant communication technologies used by commercial-off-the-shelf devices, i.e., IEEE 802.11. We describe two operational modes: (i) binary classification via Convolutional Neural Networks and (ii) one-class classification via Sparse Autoencoders. We evaluate and compare the proposed approaches with the current state-of-the-art using data collected through an extensive real-world experimental campaign in three relevant environments. At the same time, we made the dataset available to the public. Our results demonstrate that detecting weak jamming signals is feasible in all considered real-world environments, and we provide an in-depth analysis that considers different techniques, scenarios, and mobility patterns.

Keywords: Wireless Security, Artificial Intelligence for Security, Mobile Security

1. Introduction

Nowadays, jamming is one of the most simple and effective ways to disrupt the operations of wireless networks. In fact, by injecting high-power noise into the communication channel used by Radio Frequency (RF) devices, malicious parties disrupt the communications of static and mobile devices, affecting significantly large areas. As a result, devices lose the ability to communicate, leading to networking issues [1].

Several solutions are available today for detecting jamming in wireless networks [2]. However, most of such solutions detect jamming *ex-post*, i.e., after jamming has already affected the quality of the wireless communication link. For instance, consider the scenario where a mobile device (vehicle, robot, or

drone) approaches an area under jamming, thus experiencing an increasing effect of the jammer, with a growing Bit-Error-Rate (BER), which, in turn, affects the quality of the communication link. In such a scenario, it is desirable to detect jamming *earlier*, when the jamming signal is weak, and thus, not enough to break the communication link, but strong enough to be detected. Detection of weak jamming signals is also a valuable technique for large static networks, such as the Internet of Things (IoT), where nodes located on the boundaries of the jammed area can detect the presence of the (weak) jamming signal while not being affected by it—they are still able to communicate with their neighbors while being able to detect the presence of the weak jamming signal. Jamming detection in these scenarios enhances situational awareness, allowing the system administrator to switch to a safer and more robust network configuration or communication protocol. Such scenarios are sometimes referred to as *low-BER regimes* and *low-power jamming*, and to the best of our knowledge, jamming detection solutions suitable for such scenarios and validated with real-world data have been considered only by our preliminary work in [3] and [4].

Although the results reported in these works demonstrate the feasibility of detecting weak jamming in indoor scenarios, many gaps remain unresolved. In particular, it is unclear whether

*This work has been partially supported by the INTERSECT project, Grant No. NWA.1162.18.301, funded by the Netherlands Organization for Scientific Research (NWO). Any opinions, findings, conclusions, or recommendations expressed in this work are those of the author(s) and do not necessarily reflect the views of NWO. Moreover, this publication was made possible by the NPRP12C-0814-190012-SP165 award from the Qatar National Research Fund (a member of Qatar Foundation).

*Corresponding author

Email addresses: m.f.g.hanegraaf@student.tue.nl (Martijn Hanegraaf), s.sciancalepore@tue.nl (Savio Sciancalepore), g.oligeri@hbku.edu.qa (Gabriele Oligeri)

detection of weak jamming signals could also work effectively and reliably outdoors, where the multipath effect may affect the signal behavior differently than indoors. Moreover, the experiments in [3] and [4] consider only the most straightforward digital modulation technique, i.e., Binary Phase-Shift Keying (BPSK), and a *clean* communication channel. It is unclear how to generalize the solution conceived therein for more complex modulation schemes used by mobile devices in the real world, e.g., IEEE 802.11 (WiFi), working in the crowded 2.4 GHz frequency band. Finally, the technique designed in [4] requires the acquisition of a significant amount of data for training a Deep Learning (DL) model; no investigation has been conducted so far about the size of the training set and how this affects the performance of the classifier, as well as the effectiveness of data augmentation techniques.

Contribution. In this paper, we improve and extend our previous contributions in [3] and [4] through the design of general-purpose solutions to detect weak jamming signals, compatible by design with real-world digital modulation schemes used by modern Commercial Off-The-Shelf (COTS) devices. Our proposed solution converts raw Physical (PHY)-layer signals acquired from the wireless channel into images and then uses various DL-based solutions to detect jamming by correct classification of such images. We provide two operational modes of our approach, i.e., binary classification via Convolutional Neural Networks (CNNs) and anomaly detection via Autoencoders (AEs). We evaluated the effectiveness of these approaches for weak-jamming detection through an extensive real-world experimental campaign encompassing three relevant environments (indoor, outdoor with multipath, outdoor with minimal multipath) and several protocol configurations, jamming parameters, and communication parameters. As relevant results, we demonstrate that our newly proposed image generation technique is successful for weak jamming detection, and it generalizes by design with more complex modulation schemes. We also demonstrate that when detecting jamming becomes particularly challenging, CNNs outperform AEs thanks to the availability of anomalous (jamming) samples at training time. We also release the dataset collected for this study open-source at [5], fostering future research.

We highlight that this work extends further our previous studies in [3] and [4], through the following new contributions:

- We extend further the image generation methodology introduced in the previous papers [3] and [4] through the design of an enhanced image generation technique taking into account the higher complexity of the real-world modulation schemes, and we demonstrate experimentally the advantages and trade-offs connected with such a choice.
- Although previous studies evaluated weak-jamming detection only indoors, in this study, we extend our experimental analysis by carrying out extensive data collection outdoors, considering environments characterized by heterogeneous multipath conditions, and we release our data open source.
- While previous studies only consider data delivered on

custom communication frequencies (e.g., 900 MHz) through the BPSK modulation, in this study, we extend our analysis considering an actual communication technology used by wireless devices outdoors, i.e., IEEE 802.11, working on the crowded 2.4 GHz frequency band, using the Orthogonal Frequency Division Multiplexing (OFDM) modulation scheme with BPSK, Quadrature Phase-Shift Keying (QPSK), 16-Quadrature Amplitude Modulation (QAM), and 64-QAM.

- We extensively compare the performance of the proposed jamming detection techniques with the approaches previously proposed in [3] and [4] across several configurations, jamming techniques, and communication parameters.
- We investigated the problem of data set size and evaluated the performance of the classifier with different training set sizes using various data augmentation strategies traditionally used for image processing, including rotation, mirroring, contrast adjustment, and brightness adjustment. We show that some strategies contribute to keeping jamming detection accuracy high while requiring fewer real-world data.

This research demonstrates experimentally the potential and feasibility of detecting weak jamming signals in many different scenarios and operational conditions, ultimately paving the way for adopting such techniques in the wild.

Roadmap. The paper is organized as follows. Sec. 2 introduces the preliminaries, Sec. 3 reviews related work, Sec. 4 introduces our scenarios and adversarial model, Sec. 5 provides the details of the investigated methodologies for weak-jamming detection, Sec. 6 describes our data collection campaign, Sec. 7 presents the results of our analysis, Sec. 8 discusses relevant results and deployment aspects of our solutions and, finally, Sec. 9 concludes the paper.

2. Preliminaries

In this section, we introduce preliminary concepts used in our paper, i.e., digital modulation techniques (Sec. 2.1) and DL strategies for jamming detection (Sec. 2.2).

2.1. Digital Modulation

Digital modulation schemes used for modern wireless communications transform a digital bit stream to a RF signal, suitable to be transmitted over a wireless channel [6]. Such RF signal is typically expressed as a complex number of the form $s = \mathbf{I} + j\mathbf{Q}$, generally denoted as In-Phase - Quadrature (IQ) samples, where \mathbf{I} is the real component and \mathbf{Q} is the imaginary component. As an example, Fig. 1 shows (real) IQ constellation plots for the modulation schemes BPSK, QPSK, 16-QAM and 64-QAM, respectively, as obtained during the experiments carried out for this work. We notice that the higher the order of the modulation, i.e., the number of different IQ values, the higher the number of bits that an IQ sample can carry. For example,

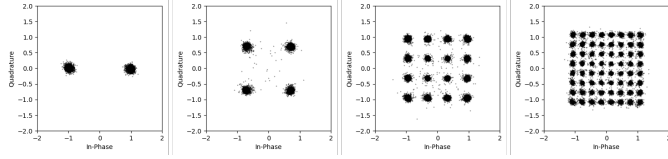


Figure 1: IQ constellations for BPSK, QPSK, 16-QAM and 64-QAM, respectively, obtained from our experiments.

each IQ sample in the BPSK scheme carries a single bit (0 or 1), while an IQ sample in the QPSK scheme carries two bits (00, 01, 10, or 11). At the same time, we also notice that the transmission of the IQ samples on the wireless channel affects their value, thus changing the original value of the sample, i.e., moving the position of the sample from the expected location in the IQ constellation plane. When the noise is low, and the shift from the expected position is minimal, errors do not affect the mapping. However, the higher the order of the modulation scheme, the greater the chance that the wireless channel moves a sample far away from the expected one, thus causing a *decoding error*. Digital modulation schemes trade off performance (throughput) with robustness to noise. In this paper, in line with our previous works in [3] and [4], we consider *Low-BER Regime* as a communication channel in which noise slightly affects the quality of the communication link, causing only a few decoding errors, below 1%. The techniques described in this paper aim to detect the presence of weak jamming signals in such challenging conditions, i.e., before jamming takes down the communication link.

2.2. Deep Learning Tools for Jamming Detection

We consider two DL-based tools for image classification, i.e., Convolutional Neural Networks and Autoencoders.

Convolutional Neural Networks. CNNs are primarily used in the field of pattern recognition within images, with the task of classifying them [7]. The input of the classifier, usually in the form of a multidimensional vector, is loaded into the input layer, which distributes it over the hidden layers. Without loss of generality, a CNN comprises three neural layers, i.e., convolutional layers, pooling layers, and fully connected layers. The convolutional layer generates various feature maps from the input using the mathematical convolution operation, producing one function from two input functions. The feature map is an abstraction of the input image. The pooling layer follows the convolutional layer and reduces the dimensions of the feature maps and network parameters. In the fully connected layer, each neuron in the previous layer is connected to each neuron in the current layer. The number of neurons in this layer usually matches the number of output classes [7]. CNNs take as input raw image pixels and outputs class scores, indicating the likelihood that the input sample is part of the specific class. Note that training a CNN requires images from all classes.

Autoencoders. AEs are neural networks designed to encode the input into a compressed representation, i.e., the latent representation, and then decode it back so that it is as similar as possible to the input [8]. The problem can be summarized by

identifying an encoder function $A : \mathbb{R}^n \rightarrow \mathbb{R}^p$ and a decoder function $B : \mathbb{R}^p \rightarrow \mathbb{R}^n$ that satisfy Eq. 1:

$$\arg \min_{A, B} E[\Delta(\mathbf{x}, B \circ A(\mathbf{x}))], \quad (1)$$

where E represents the expectation over the distribution of x , \circ is the composition operator, and Δ is the function that measures the distance between the input and the output of the decoder, called the reconstruction loss function. In the cybersecurity research domain, AEs have been used successfully for anomaly detection [9], [10]. Let J and K be two probability distributions such that $J \neq K$ and let c be an AE model trained on samples from J . When using c to reconstruct samples, we expect a smaller reconstruction error on samples from J than unseen samples from K [11]. We can identify a specific reconstruction error value and use it as a threshold value τ , defining a boundary for classification. Any input sample to c with a reconstruction error greater than τ can be classified as $\notin J$, i.e., an anomaly. Note that, differently from CNNs, AEs require only one class for training, i.e., the samples of the *legitimate* class (no anomalies). In Sec. 5, we discuss in more detail what such a feature entails for jamming detection.

3. Related Work

Several jamming detection approaches have been proposed in the scientific literature, as discussed in recent surveys such as [1] and summarized in Tab. 1. Jamming detection is usually performed by analyzing one or more communication link metrics, e.g., the Packet Delivery Ratio (PDR), the Packet Loss Ratio (PLR) and Packet Rejection Ratio (PRR). Some approaches detect jamming through the analysis of PHY-layer metrics, such as the Received Signal Strength (RSS) [29], while others consider the analysis of raw signals, represented in different ways. For example, the authors in [17] pre-process IQ samples with a Stockwell Transform (ST), while the authors in [16] extract the spectrogram from the raw signal, and the authors in [22] use the Short-Time Fourier Transform (STFT) and the Complex Gaussian Derivative Wavelet Transform (CGDWT) to extract more information from the raw signal. Others use the Chip Error Rate (CER), which is derived from the chip-to-symbol conversion process [21], the Residual Energy Decay Rate [18] or the Logarithmic Received Energy [19]. In contrast to using only one feature, multiple heuristic signal processing features can also be used, as discussed in [24].

The recent increased popularity of Artificial Intelligence (AI) has contributed to an increase in the usage of Machine Learning (ML)- and DL-based approaches for the analysis of the chosen link metric(s). We can notice a great variety in the usage discriminative AI-based tools, including Random Forests [15, 16, 20], K-Nearest Neighbors (K-NN) [24], CNN [16, 3], Deep CNN, Deep Recurrent Neural Networks [22] and Sparse AEs [4]. A generative ML model, Conditional Generative Adversarial Network (C-GAN) is used in [17]. There are also attempts to use non-ML based approaches, such as the Heuristic Hypothesis Test (HHT) [21] and Hidden Markov Models (HMMs) [19]. Some recent papers, such as [30] and [31], considered

Table 1: Qualitative comparison of relevant literature on jamming detection. Duplicated rows with the same reference indicate multiple proposals by the same paper. For evaluation setup, ● indicates Indoor and Outdoor evaluation, ◐ indicates Indoor or Outdoor, and ○ indicates simulation or analytical evaluation. The symbol - indicates that the paper provides no information about a specific feature. The works [12], [13], and [14] are not reported since, although applying image generation from RF signals, they do not deal with jamming detection.

Ref.	Metric	Technique	Communication Technology	Modulation Scheme	Jamming Signal	Robustness to Distance	Weak Jamming	Jamming Knowledge	Eval. Setup	Robustness to Mobility
[15]	IT, PDR, RSSI	RF	IEEE 802.11	OFDM	BPSK	○	○	○	●	●
[16]	Spectrogram	CNN	IEEE 802.11	OFDM	AWGN, Tone, Pulse, OFDM	○	○	○	●	○
[16]	SNR, RSSI, OFDM-Specific	RF	IEEE 802.11	OFDM	AWGN, Tone, Pulse, OFDM	○	○	○	●	○
[17]	ST	C-GAN	5G	B/QPSK, 16/64-QAM	AWGN	○	○	●	●	○
[17]	I/Q	DBN	5G	OFDM	OFDM	○	○	○	○	○
[18]	Res. Energy Decay Rate	ML	-	QAM, PAM, FSK, PSK	AWGN	○	○	○	○	○
[19]	Log. Received Energy	HMM	-	-	AWGN	○	○	●	○	○
[20]	BPR, PDR, RSSI, CCA	RF	5G	-	AWGN	○	○	○	●	○
[21]	CER	HHT	IEEE 802.15.4	DSSS	DSSS	○	○	●	●	●
[22]	STFT, CGDWT	DCNN, DRNN	-	OFDM	AWGN, OFDM	○	○	○	●	○
[23]	Timing Resource Alloc.	DBN	4G	OFDM	OFDM	○	○	○	○	○
[24]	Heuristic Proc. Features	K-NN	IEEE 802.11p	OFDM	AWGN	○	○	○	●	○
[25]	RSS	Effective Radiated Power Game Theory	WiMAX	DSSS	Pulse Sweep Single-band	○	●	○	○	○
[26]	Time	-	-	-	AWGN	○	●	●	○	○
[27]	Packet Drop Probability Spectrogram	SVM, Random Forests	IEEE 802.11	OFDM	AWGN	○	●	○	○	○
[28]	-	PCA	IEEE 802.11	OFDM	AWGN	○	●	○	●	○
[3]	I/Q	CNN	-	BPSK	BPSK	●	●	○	●	○
[4]	I/Q	AE	-	BPSK	AWGN, BPSK	●	●	●	●	○
This paper	I/Q	CNN, AE	IEEE 802.11	OFDM w/ B/QPSK, 16/64-QAM	AWGN, BPSK	●	●	●	●	●

the problem of jamming classification at the PHY layer, especially in the context of satellite signals. However, such papers aim to detect and classify jamming, not to identify it when its power is low compared to the communication signal. Similarly, the authors in [32] investigated the resilience of satellite fingerprinting schemes to jamming while not investigating jamming detection.

In this paper, we focus on the detection of *weak* jamming, i.e., detecting jamming in a situation where the level of the received jammer power at a target is not enough to shut down the communication link entirely but only to affect it slightly. In our earlier contributions, we denoted such a scenario as a *Low-BER Regime* since it translates into a low (non-zero) BER at the target. We notice that weak-jamming detection is relevant for static and mobile networks. Mobile devices, such as with Unmanned Aerial Vehicles (UAVs) and autonomous vehicles, could detect jamming while moving toward the jammer's location. In these contexts, weak-jamming detection enables the pilot and the Ground Control Station (GCS) to keep control of the vehicle rather than losing control and relying on a pre-programmed action to navigate safely. Although some works in the literature consider tests for jamming under mobility, e.g.,

[15] and [21], to the best of our knowledge, only a few papers delved into the detection of weak and low-power jamming and proposed solutions to this problem. The pioneering contribution by GarnaeV et al. in [26] only provided numerical analysis, while the contributions by Boganoski et al. [25] and Venkata et al. [27] used simulations to prove the feasibility of detecting low-power jamming. The authors in [27] used SVM and Random Forest classifiers to detect jamming, identifying early the potential of ML to address this problem. However, they considered the scenario of vehicular networks and their proposed methods took significant time (in the order of seconds), not being suitable to highly dynamic conditions. More recently, Villain et al. [28] were the first to use real-world data collected in an office environment to show that, using Principal Component Analysis (PCA), it is possible to detect low-power jamming. Such works mostly focus on spectral differences, while providing limited quantitative results across various jamming detection parameters. Indeed, they do not consider the impact of the distance between transmitter, receiver and jammer, and not even mobile deployments. They also consider an external device specifically meant for jamming detection. A step further in this direction is offered by our recent

contributions in [3] and [4], which cover many different properties of low-power-jamming detection, including the impact of the distance between the jammer and the communication link. They are also the only contributions releasing the data and the code used for their experiments, encouraging reproducibility. Although using real-world data, those contributions consider simple communication links, not aligning with real-world operational environments, and test their solutions indoors. In this paper, we advance further the state of the art on weak-jamming detection by (i) extending the methodology defined in [3] and [4] for more complex modulation schemes; (ii) using an actual communication technology used by many wireless deployments, including drones and connected vehicles, i.e., WiFi, (iii) evaluating weak-jamming detection with various modulation schemes used in the real-world WiFi, i.e., OFDM with BPSK, QPSK, 16-QAM and 64-QAM, and (iv) performing extensive tests outdoors, considering various signal propagation conditions (indoors, outdoor garden and outdoor field). Moreover, compared to early works on low-power jamming detection, this paper makes significant advancements: (i) extensive real-world data collection, (ii) extensive experiments and results considering various jamming detection parameters, (iii) use of state-of-the-art DL-based solutions, and (iv) very limited collection and inference time, applicable to real-time scenarios. Finally, we highlight that the image generation technique used in our paper shares similarities with the one recently used for Radio Frequency Fingerprinting (RFF), e.g., in [12], [13], and [14]. The proposal in [12] is meant to detect spoofing attacks to satellite constellation through the analysis of the physical-layer information available at the receiver. To this aim, the authors generated images from IQ samples and applied classification to detect spoofing attacks. The authors in [13] showed that the power-cycles of the radios affect the performance of RFF solutions, and that techniques based on images can improve performance compared to analyzing raw physical-layer data. The authors in [14] show that Adversarial Machine Learning techniques can be used to improve the robustness of image-based RFF techniques, so avoiding synthetic attacks via imitation of the features of the physical-layer signals at a receiver. However, using such image generation technique for the detection of weak jamming entails different choices and analysis methods, not affecting the novelty and aim of our contribution.

4. Scenario and Adversary Model

Figure 2 depicts the reference scenarios and the adversary model considered in this work.

We consider two reference scenarios, i.e., Fig. 2(a), representing a mobile receiver (RX) moving towards a jammed area while communicating with a remote transmitter (TX), and Fig. 2(b), showing a partially jammed dense network of Internet of Things (IoT) devices, simultaneously acting as TX and RX. For both scenarios, the presence of the jammer splits the playground into three areas: A_1 , A_2 , and A_3 , respectively. No message reception is possible in the area A_1 as the jamming signal overcomes the power of the legitimate signal of the transmitter. In contrast, communication is possible in areas A_3 and A_2 ,

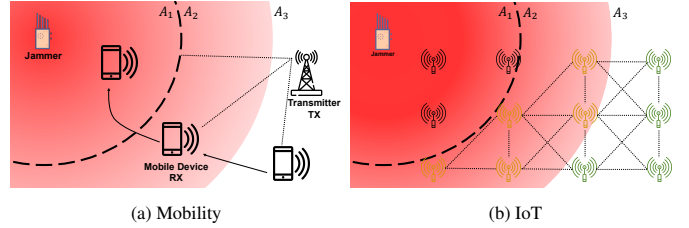


Figure 2: System and Adversary Model. Our solution applies to two reference scenarios. (a) A receiver (RX) moves from area A_3 to area A_2 and eventually to A_1 . RX can receive messages from TX when in A_2 and A_3 , while reception is not possible in A_1 due to jamming. (b) A dense network is partially jammed (black devices in A_1) while (yellow and green) devices in A_2 and A_3 can communicate.

but in A_2 , the devices experience both the legitimate signal and the jamming. In particular, devices deployed in A_2 can infer the presence of a jammer through the analysis of the received signal at the PHY layer.

Without loss of generality, we consider that the RX (IoT) device features an omnidirectional transceiver antenna, in line with the equipment onboard regular wireless devices. We consider the IEEE 802.11g communication technology based on its common usage in several COTS IoT devices. We recall that IEEE 802.11g works in the 2.4GHz ISM band and supports the following modulation schemes: OFDM with BPSK, QPSK, 16-QAM and 64-QAM.

Adversary Model. We consider an adversary \mathcal{A} equipped with an omnidirectional antenna that emits a jamming signal to disrupt the radio communication nearby (area A_1). The jamming signal can be noise, i.e., Additive White Gaussian Noise (AWGN), or deceptive, i.e., adopting the same modulation scheme used by the legitimate communication link. We notice that deceptive jamming assumes some level of prior knowledge about the communication link. Furthermore, we consider an adversary that constantly jams at the highest possible transmission power. The usage of the highest transmission power is consistent with the general consideration that the jammer wants to prevent any communication in the nearby area as much as possible while not knowing the specific location of the RX and the TX. We also consider a jammer unaware of the sampling rate used by the legitimate communication link. Thus, it transmits the jamming signal with the highest possible sampling rate as a function of the available hardware. Note that weak-jamming occurs even when the jammer emits jamming with high power: indeed, if the receiver is sufficiently farther away, the level of the injected noise is not enough to jam the channel completely, creating a weak-jamming scenario.

Finally, we highlight that area A_2 is characterized by a bit error rate below 1%. This is the area that we will focus on in this work. In fact, in this region, the RX (IoT) wireless device can (potentially) detect the presence of the jammer and has a reliable communication link with the TX, thus allowing awareness and informed decisions on the following actions. Detecting weak jamming signals increases situational awareness and allows the TX to take action accordingly without having to rely on pre-defined backup steps pre-programmed on the RX device.

Table 2: Notation and brief description.

Notation	Description
P, Q	Image dimensions (Width, Height).
n	Number of IQ samples per image.
τ	Threshold value for the AE.
$MS E_{train}$	MSE value from reconstructing the trainset.

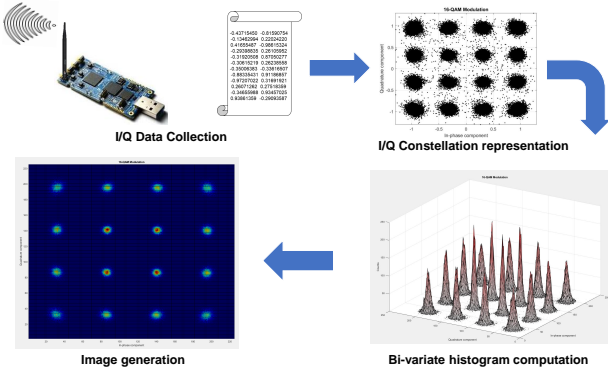


Figure 3: We collect the IQ data through a Software-Defined Radio (SDR), then divide them into chunks of n samples per image, represent them in a constellation diagram, compute a bi-variate histogram, and store it as an image.

5. Detection of Weak Jamming Signals

In this section, we introduce our enhanced methodology for weak-jamming detection. Overall, we can identify two main phases, i.e., *Image Generation* (Sec. 5.1) and *Jamming Detection* (Sec. 5.2). Tab. 2 summarizes the main notation used throughout the section.

5.1. Image Generation

Figure 3 presents an overview of the adopted image generation pipeline. We collect IQ samples using a device capable of acquiring PHY-layer wireless channel information, e.g., an SDR. Next, we divide these samples into subsets of n samples, denoted as the *number of samples per image* (see Sec. 7 for details on the impact of this parameter on jamming detection). Then, we represent each subset of n IQ samples through the IQ constellation diagram, with the *In-phase* component on the x-axis and the *Quadrature* component on the y-axis. We highlight that our image processing technique differs from the previously proposed approach, being more suitable for higher-order modulation schemes. Previous solutions [3] and [4] considered only one of the two clouds in the image. In contrast, we consider the IQ constellation with x-axis and y-axis limits of $[-2, 2]$ and divide it into a $P \times Q$ grid. Note that, at the receiver, we normalize the value of the IQ samples, thus ensuring that their values do not fall outside of the considered range. We apply dataset-level normalization, i.e., we compute the maximum values of raw I and Q (I_{MAX}, Q_{MAX}), and we normalize the samples as $I = \frac{I}{I_{MAX}}$ and $Q = \frac{Q}{Q_{MAX}}$. We use the mentioned grid to generate a bi-variate histogram by counting how many IQ samples fall into a specific tile of the grid. The bins in the histogram are considered to be the value of the image pixels. Lastly, the output of the histogram is saved as a $P \times Q$ grayscale image, where P and

Q are selected based on the input requirements of the classifier used later in the jamming detection phase. In Sec. 7, we experimentally compare the proposed image generation method with the technique used in [3] and [4] and evaluate the pros and cons.

5.2. Jamming Detection

We consider two different approaches, i.e., binary classification using CNNs, as in [3], and anomaly detection using *sparse AEs*, as in [4]. While the former requires the knowledge of samples affected by jamming, the latter can be deployed in scenarios where jamming has never been observed during the training of the model, reducing the training overhead.

Binary Classification via CNNs. This approach detects jamming based on a binary classifier. More in detail, we use a CNN with 18 residual layers, i.e., ResNet-18 [33] which is pre-trained on the ImageNet dataset [34]. We adapt the CNN to have two output classes to distinguish between jamming and no jamming. We present a simplified visual overview of the architecture in Fig. 4. We consider a training process charac-

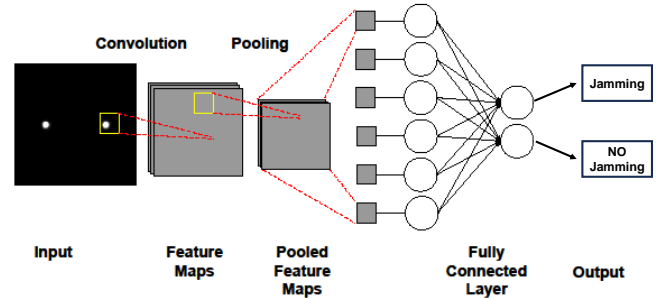


Figure 4: Visual representation of a the CNN used for binary jamming detection.

terized by 30 epochs and a mini-batch size of 35 elements. We use images generated from IQ samples captured with no jamming affecting the communication link (*NO JAM* images) and an equal number of images generated from IQ samples captured with jamming (referred to as *JAM* images) for the training process. The final output of the algorithm is the decision between jamming or no jamming. For hyper-parameters tuning, we referred to the same configuration used in [4].

Anomaly Detection via AEs. This approach detects jamming by identifying anomalies in the received signal, using sparse AEs. Figure 5 shows the adopted AE architecture. We consider the generated images as described in Sec. 5.1 as input of an encoder using a logarithmic sigmoid function with $K = 16$ neurons, obtaining a compressed latent representation of the input image consisting of $K = 16$ dimensions. Then, we feed the latent representation vectors to a decoder using a linear decoder transfer function with a total number of $J = 50, 176$ neurons, as described in [4]. We use two hidden layers and the sparsity regularization technique in line with the methodology provided in [4]. The output is an image of the same size as the input image ($P \times Q$). We convert this image into a matrix and compare it with the input through the Mean Squared

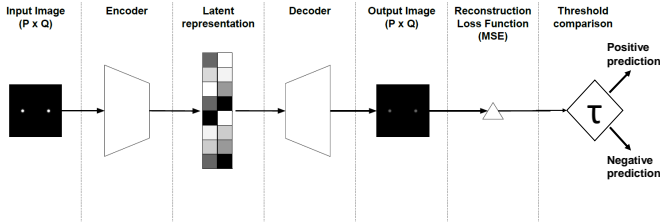


Figure 5: Visual representation of the AE-based jamming detection architecture.

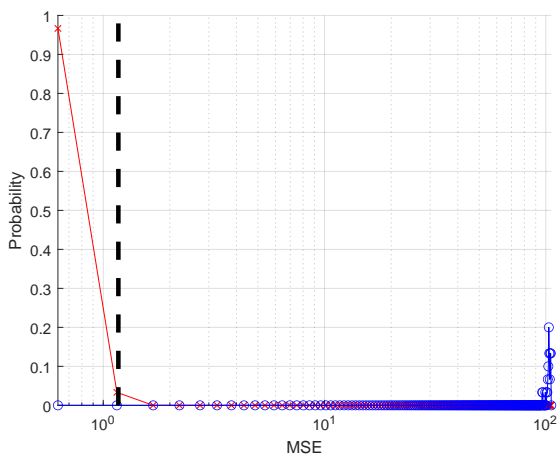


Figure 6: Sample distribution of the MSE values from our dataset, with *NO JAM* images (red), *JAM* (blue) images, and threshold value (dashed line).

Error (MSE) loss function. This approach entails *training* and *testing*. For the training process, we use images generated from IQ samples captured with no jamming affecting the communication link, generating a set of MSE values representing the regular behavior of the link. We use these values to calculate the threshold τ to differentiate images generated from non-jamming or jamming samples. An image with $MSE < \tau$ is predicted to be generated from no jamming samples, while an image with $MSE > \tau$ is predicted to be generated from jammed samples. For computing τ , we adopt Eq. 2, as proposed by the authors in [35].

$$\tau = E(MSE_{train}) + 3.5 \cdot \sigma(MSE_{train}), \quad (2)$$

where $E(\circ)$ and $\sigma(\circ)$ represent the mean and the standard deviation, respectively.

An image generated from unjammed samples is characterized by lower MSE values. In contrast, an image generated from jammed samples results in a higher MSE value. We show a sample distribution of the MSEs in Fig. 6. Finally, note that we select the same values for the hyperparameters of the AE and CNNs as the approach presented in [4], i.e., a hidden size value of 16, a sparsity regularization term of 0.5, an L2-regularization term of 0.01, the Logistic Sigmoid (logsig) function as the en-

coder transfer function and 250 epochs for the training process.

6. Data Collection and Experiment Settings

In this section, we describe the methodology used for data collection, including the hardware and software details of our measurement setup (Sec. 6.1) and the settings used for the experiments (Sec. 6.2).

6.1. Hardware and Software

Hardware. We consider the SDRs provided by Lime Microsystems, i.e., three LimeSDR USB [36] devices and one LimeSDR Mini v2.0 [37], equipped with a WiFi-capable antenna and an up-to-date firmware. The LimeSDR USB has a frequency range of 100 kHz up to 3.8 GHz, a maximum bandwidth of 61.44 MHz, and a transmit power of up to 10 dBm. The LimeSDR Mini V2.0 has a smaller frequency range of 10 MHz up to 3.5 GHz, 40 MHz of maximum bandwidth, and a maximum transmitting power of 10 dBm. We use two LimeSDR USB devices to establish an RF communication link, thus representing the GCS and UAV. Another LimeSDR USB and the LimeSDR Mini v2.0 are used as jammers to disrupt the communication link. We use two general-purpose laptops to control the SDRs. For data analysis, we upload the captured IQ samples to a centralized computing facility, i.e., the High-Performance Computing (HPC) cluster hosted at TU/e, Eindhoven, Netherlands. It provides an AMD EPYC 7313 CPU running at 3.00 GHz, 16 GB of RAM, and an NVIDIA A30 GPU with 24GB of RAM.

Software. We use GNUradio version 3.10 [38] and the block *gr-limesdr* [39] to interact with the SDRs. The block diagram used for this work builds on top of the publicly available out-of-tree module *gr-ieee-802-11*, available at [40], allowing the transmission and reception of IEEE 802.11g packets through SDRs, with a few relevant modifications. Specifically, to make the block diagram work correctly on our hardware, we added two blocks to the receiver chain, i.e., an *FFT Filter* and *DC Spike Remover*. Such modifications filter out the DC offset affecting the used hardware and make it possible to correctly receive IQ samples. We also save the IQ data corresponding to correctly received WiFi packets to a file, in the *fc16* format, useful for post-processing according to the techniques described in Sec. 5. We also modify the block diagram of the WiFi transmitter by adding a block *Multiply Const* just before the block *LimeSDR Sink*, with an input value of 0.5. This modification is meant to reduce the amplitude of the resulting signal and make it transmittable by the LimeSDR without distortions. On the receiving LimeSDR, we collect the IQ samples corresponding to the whole IEEE 802.11g packet, including both the header and payload. We collect IQ samples from the wireless channel using a limited sample rate of $5 \cdot 10^6$ samples per second (sps), as the link becomes unreliable at higher sample rates (see Sec. 8 for a discussion of the impact of this choice on our results). We consider a transmission rate of one IEEE 802.11g frame every 15 ms, bounded by the capabilities of our hardware. The payload consists of two x characters. For the jammer, we use the

blocks *Gaussian Noise Source* to generate samples, *Multiply Const* with input value 0.5 to avoid RF signal distortion, and *LimeSDR Sink* to transmit the samples to the hardware. As for the implementation of the deceptive jamming, we consider the same flow diagram used for the transmitter. Finally, note that we set the carrier frequency for all SDRs to $f_c = 2,484$ MHz, equal to channel 14 as described by IEEE 802.11g [41].

6.2. Measurement Settings

Table 3 provides the details of the dataset collected for this work. It describes, for each environment, the tested control variable, experiment-specific settings, tested jamming conditions, collected IQ samples, dataset size, and Symbol Error Rate (SER). Note that we collected over 6.6 GB of data and 843M+ IQ data. To the best of our knowledge, this is the largest dataset for weak jamming scenarios including both indoor and outdoor measurements.

We consider three different measurement environments characterized by an increased amount of background noise, namely, Outdoor Low-Multipath (E1), Outdoor Multipath (E2), and Indoor (E3).

E1: Outdoor Low-Multipath. This environment is a wild field in the countryside, as shown in Fig. 7, with no obstructions in a radius of 100 m. The possibility of multipath fading is minimized, although the signal could still reflect from the ground.

E2: Outdoor Multipath. This environment is a large garden with trees, plants, and a shed, as shown in Fig. 8. Here, multipath is likely to occur due to the obstacles located very close to the deployment location of the devices.

E3: Indoor. This is an office-like environment with a table, chairs, and windows, depicted in Fig. 9. Due to the presence of walls, the RF signal is reflected and attenuated. We schematize



Figure 7: Picture taken at E1 (Outdoor Low-Multipath). The X and arrow on the satellite image (top right) indicate testing location and direction.

the reference setup of the devices in the experiments in Fig. 10.

The relative position of the transmitter, receiver, and jammer changes as a function of the scenario considered due to our requirement for weak jamming of the communication link. In the reference scenario, the jammer is in the same position as the transmitter, while both are 5 meters from the receiver.



Figure 8: Picture taken at E2 (Outdoor Multipath). The X and arrow on the satellite image (top left) indicate testing location and direction.

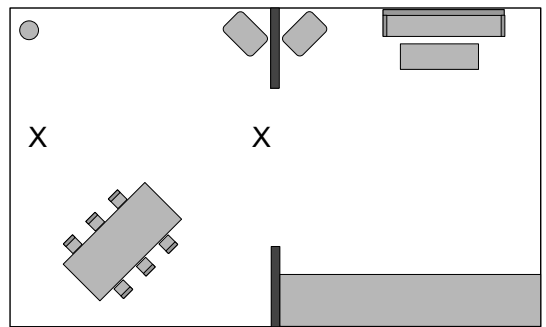


Figure 9: Layout map for E3 (Indoor). The symbols X indicate testing locations. The room contains a coathanger (top left), two wood stoves (top center), a table with chairs (bottom left), two walls (top and bottom center), a couch with a table (top right), and a kitchen (bottom right).

In the Low-SNR scenario, the distance between the transmitter and the receiver is still 5 meters, but the jammer is deployed closer to the receiver (1.5 meters). Finally, in the Modulation scenario, all the devices are 1.5 meters away from a reference point. We considered two channel conditions for each setup, namely, without jamming (NO JAM) and with jamming (JAM). By default, we took measurements lasting 15 minutes for the JAM scenario and 30 minutes for the NO JAM scenario. For the reference setup, we set the gains on the TX, RX, and Jammer to 62, 50, and 44, respectively. These values allow for a stable and reliable communication link, a fundamental condition for our tests.

We highlight that reproducing *weak jamming* conditions in real-world scenarios is challenging. Indeed, each environment (indoors, outdoors w/o multipath) is characterized by peculiar propagation conditions, which affect the impact of the jammer on the legitimate communication link. Moreover, our measurements have been executed in regular operational conditions, with people and vehicles moving around the communication link and other networks coexisting on the same spectrum. Therefore, it is not possible to control precisely the communication channel—this would also be unfair, since we consider real-world communication environments. Therefore, all our experiments consider as a *base condition* a situation where the BER of the legitimate communication link under jamming (JAM) is not more

Table 3: Details of the dataset collected as part of our experiments.

Env.	Control Variable	Jamming Conditions	Experiment-specific Settings	Collected IQ Samples	Dataset Size [MB]	SER
E1	Jammer Distance	No Jam		80740310	61.6	0,0583
		Jam	3, 5, 7, 10, 13, 16, 19, 21, 23, 25 m	43729434	309.35	0,0663
	Receiver Distance	No Jam	5, 7, 10, 13, 16, 19, 21, 23, 25, 27 m	7986299	633.52	0,0008
		Jam	5, 7, 10, 13, 16, 19, 21, 23, 25, 27 m	43950176	343.37	0,0107
	Transmitter Distance	No Jam	5, 7, 10, 13, 16, 19, 21, 23, 25, 27 m	79805862	623.49	0,0127
		Jam	5, 7, 10, 13, 16, 19, 21, 23, 25, 27 m	47540014	371.43	0,0330
	Reference Setup	No Jam	Location 0 (Ref. Setup)	8074310	63.08	0,0583
	Jammer Gain	Jam	6, 12, 14, 16, 18, 20	24160008	188.75	0,0821
	Jammer Location	Jam	1, 2, 3	12112545	94.63	0,0763
	Jamming Oversampling Ratio	Jam	1, 2, 3, 4	16150765	126.18	0,0788
Jammer Type	Jam	AWGN, Deceptive	12185053	94.5	0,4287	
E2	Reference Setup	No Jam	0, 3 m	16769451	131.01	0,0542
	Jammer Distance	Jam	3, 5, 7, 10, 13, 16, 19, 21, 23, 25, 27 m	47542742	371.42	0,0823
	Receiver Distance	No Jam	5, 7, 10, 13, 16, 19, 21 m	59417153	464.17	0,0526
		Jam	5, 7, 10, 13, 16, 19, 21 m	30666679	239.58	0,1899
	Transmitter Distance	No Jam	5, 7, 10, 13, 16, 19, 21 m	59417153	464.17	0,1256
		Jam	5, 7, 10, 13, 16, 19, 21 m	30389065	237.4	0,0917
	Reference Setup	No Jam		7951440	62.12	0,0302
	Jammer Gain	Jam	24, 26, 28, 30, 32	16312240	155.41	0,0244
	Jammer Location	Jam	1, 2, 3	12119906	94.68	0,0838
	Jamming Oversampling Ratio	Jam	1, 2, 3, 4	16160104	126.25	0,0719
Jammer Type	Jam	AWGN, Deceptive	11887393	92.17	0,4408	
E3	Jammer Hardware	Jam	LimeSDR Mini, LimeSDR USB	8080602	63.14	0,0652
	Modulation Type	Jam	BPSK, QPSK, 16-QAM, 64-QAM	0	79.79	0,0000
	RX Mobility	No Jam	0, 1, 2	27696974	216.38	0,0026
		Jam	0, 1, 2	14032334	109.64	0,0158
	Reference Setup	No Jam		7957589	60.7	0,0392
	Jammer Gain	Jam	6, 12, 14, 16, 18, 20	19897284	152	0,0391
	Jammer Location	Jam	1, 2, 3	12116831	92.4	0,0744
	Jamming Oversampling Ratio	Jam	1, 2, 3, 4	16163242	123.3	0,0668
	Jammer Type	Jam	AWGN, Deceptive	12200389	94.61	0,0900
	Jammer Hardware	Jam	LimeSDR Mini, LimeSDR USB	8077193	63.1	0,1024
Transmitter Gain	Jam	42, 47, 52, 57	31840829	248.75	0,0697	
Total				843131369	6652.09	

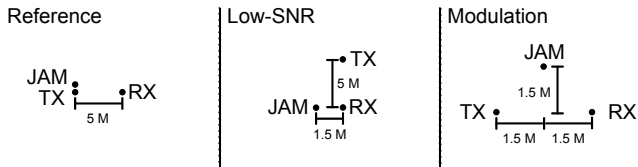


Figure 10: Scenario considered in our measurement campaign: Reference setup (left), Low-SNR (middle), and Modulation (right) physical setup.

than 1% higher than the BER of the legitimate communication link without jamming (NO JAM). Such a condition, achieved by regulating the jammer gain, allows us to experience the *weak jamming* scenario and investigate what are the capabilities to detect jamming of our proposed solutions and the techniques in the current literature.

Starting from the reference setup, for our tests, we investigate the following factors: (i) image generation parameters, (ii) jammer parameters, and (iii) communication link parameters. All data collected as part of this work are available at [5], while we provide relevant results of our experiments in Sec. 7.

7. Experimental Results

This section shows the results of our experiments. We first introduce the main performance metrics in Sec. 7.1, and then present the results about the impact on jamming detection of various image generation parameters (Sec. 7.2), jammer parameters (Sec. 7.3), and communication parameters (Sec. 7.4).

Finally, we evaluate the overhead of our solution in Sec. 7.5. We summarize the details of the experiments in Tab. 4. Note that we do not aim to compare environments across them, but to show that detecting weak jamming signals is possible in all environments across various configuration and communication parameters.

7.1. Performance Metrics

We use *accuracy* as the main performance metric, computed as $\frac{TP+TN}{TP+FP+TN+FN}$, being *TP* the number of true positives (*JAM* images correctly classified), *TN* the true negatives (*NO JAM* images correctly classified), *FP* the number of false positives (*NO JAM* images classified as *JAM*) and *FN* the number of false negatives (*JAM* images classified as *NO JAM*). Although such data are available, we do not report precision and recall results since we are interested in comparing the overall performance of the investigated approaches rather than the contribution of False Positive and False Negative. To obtain our results, we use K-fold cross-validation with $K = 5$ and, for each value, we report the mean and 95% confidence intervals, computed using Matlab's *tinv* function, i.e., the inverse cumulative distribution function of the Student's distribution. The confidence intervals are represented as red error bars in the bar plots, with a different color for each result in the line plots. To ensure fairness of comparison between CNNs and AEs, we used the same amount of images for training both classifiers, i.e. 150 *NO JAM* images. Then, for each experiment, the testing set is constituted by an equal number of *NO JAM* and *JAM* images, depending the amount of jamming data available for the particular exper-

Table 4: Details of the experiments.

	Exp.	Control Variable	Envs.	Values	Other parameters	Approaches
Image Gen. Parameters	1	No. of samples per image	E2	$10^4, 5 \cdot 10^4, 1 \cdot 10^5$	Jammer Gain=32; TX Gain= 62; RX Gain= 50	Alhazbi et al. [3], Sciancalepore et al. [4], Ours - CNN, Ours -AE
	2	Training Set Size	E2	2,9,18,36,54,72,120	Samples per image= $1 \cdot 10^5$; Jammer Gain=44; TX Gain= 62; RX Gain= 50	Alhazbi et al. [3], Sciancalepore et al. [4], Ours - CNN, Ours -AE
	3	Augment. Strategy	E2	180-deg. rot., left-right mirror, up-down mirror, contrast, brightness	Samples per image= $5 \cdot 10^4$; Jammer Gain=44; TX Gain= 62; RX Gain= 50	Alhazbi et al. [3], Sciancalepore et al. [4], Ours - CNN, Ours -AE
Jamming Parameters	4	Jammer Oversamp. Ratio	E1, E2, E3	1, 2, 3, 4	Samples per image= $1 \cdot 10^5$; Jammer Gain=44; TX Gain= 62; RX Gain= 50	Ours - CNN, Ours -AE
	5	Jammer Hardware	E2, E3	LimeSDR Mini LimeSDR USB	Samples per image= $1 \cdot 10^5$; Jammer Gain=44; TX Gain= 62; RX Gain= 50	Ours - CNN, Ours -AE
	6	Jammer Signal Type	E1, E2, E3	AWGN, Deceptive	Samples per image= $1 \cdot 10^5$; Jammer Gain=44; TX Gain= 62; RX Gain= 50	Ours - CNN, Ours -AE
	7	Jammer Location	E1, E2, E3	1, 2, 3,	Samples per image= $1 \cdot 10^5$; Jammer Gain=44; TX Gain= 62; RX Gain= 50	Ours - CNN, Ours -AE
	8	Jammer Distance	E1, E2	3, 5, 7, 10, 13, 16, 19, 21, 23, 25	Samples per image= $1 \cdot 10^5$; Jammer Gain=44; TX Gain= 62; RX Gain= 50	Alhazbi et al. [3], Sciancalepore et al. [4], Ours - CNN, Ours -AE
Commun. Parameters	9	Mod. Scheme	E2	BPSK, QPSK, 16-QAM, 64-QAM	Samples per image= $1 \cdot 10^5$; Jammer Gain=66,50,16; TX Gain= 62; RX Gain= 50	Alhazbi et al. [3], Sciancalepore et al. [4], Ours - CNN, Ours -AE
	10	Trans. Gain	E2, E3	[50, 55, 60, 65], [44, 49, 54, 59]	Samples per image= $1 \cdot 10^5$; Jammer Gain=44; TX Gain= 14; RX Gain=50;	Alhazbi et al. [3], Sciancalepore et al. [4], Ours - CNN, Ours -AE
	11	Recv. Dist.	E1, E2	5, 7, 10, 13, 16, 19, 21, 23, 25, 27	Samples per image= $1 \cdot 10^5$; Jammer Gain=66,50,16; TX Gain= 62; RX Gain= 50	Alhazbi et al. [3], Sciancalepore et al. [4], Ours - CNN, Ours -AE
	12	Recv. Mob.	E2	Static, Parallel, Perpendicular	Samples per Image= $1 \cdot 10^5$; Jammer Gain=44; TX Gain=62; RX Gain=50.	Alhazbi et al. [3], Sciancalepore et al. [4], Ours - CNN, Ours -AE

iment. This number can be obtained from Tab. 3, dividing the number of IQ samples for each environment and testing conditions by the number of samples per image used. The remaining part of the *NO JAM* dataset has been used for validation.

For some plots, we introduce a custom metric, i.e., the *Signal to Noise Ratio (SNR) Degradation Ratio*, typically presented as the second x-axis. The *SNR Degradation Ratio* models the impact of jamming on the communication channel, and it is computed as the ratio between the average SNR of the *JAM* images and the average SNR of the *NO JAM* images, i.e., $SNR_{DR} = \frac{SNR_{JAM}}{SNR_{NOJAM}}$. Note that, due to different factors affecting SNR, the *SNR Degradation ratio* is not comparable across different experiments. Finally, whenever not specified, we use only measurements characterized by a BER < 0.01, so to enforce a *low-BER* scenario following the definition in Sec. 2.

7.2. Image Generation Parameters

In the following subsection, we investigate the impact of various image generation parameters on jamming detection ac-

curacy, including samples per image, training set size, and image augmentation strategies.

Exp. 1: Samples per Image. To provide insight into the effect of the number of samples per image n on the accuracy of jamming detection, we carried out experiments for $n \in [1^4, 5^4, 1^5]$. At any higher values for n , the number of images produced is too small to allow meaningful results. Figure 11 shows the accuracy as a function of the number of samples per image while comparing our solutions (CNN and AE) with the state of the art [3] and [4], considering our reference setup for environment *E2* and a jammer gain value of 32.

We notice that the higher the number of samples per image, the higher the accuracy for all approaches. Specifically, the CNN-based approach improves from an accuracy of 0.9 with 10^4 samples per images to an average accuracy of 0.98 with 10^5 samples. Similarly, the AE-based approach improves from 0.58 with 10^4 samples to 0.995 with 10^5 samples. We notice that the CNN-based approach requires fewer samples to reach very high accuracy (higher than 0.95), i.e., $5 \cdot 10^4$ samples per image.

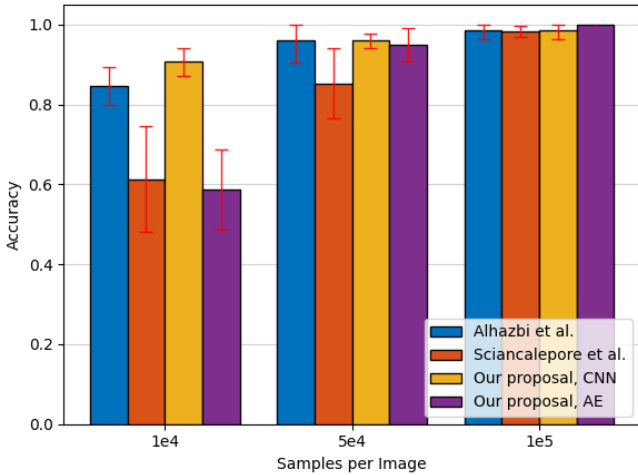


Figure 11: Accuracy as a function of the number of samples per image. We compared our proposed solutions with state-of-the-art contributions.

In such conditions, we also notice that our proposed approach significantly outperforms both previous solutions. We adopted 10^5 samples per image for the rest of our analysis. Consider that we collected data with a sample rate of $5 \cdot 10^6$ sps. Thus, the time necessary to collect 10^5 samples to generate an image is $\frac{1 \cdot 10^5}{5 \cdot 10^6} = 0.02$ s, making our solution very suitable for real-time jamming detection.

Exp. 2: Training Set Size. We also investigate the impact of the training set size on the classification accuracy. The training strategy of the two approaches is different. When the AE-based anomaly detection approach uses s images for training, such images are all images built from non-jammed samples; instead, when the CNN-based binary classification approach uses s images, we use $\frac{s}{2}$ images for both jamming and no-jamming. We report the results of our investigation in Fig. 12.

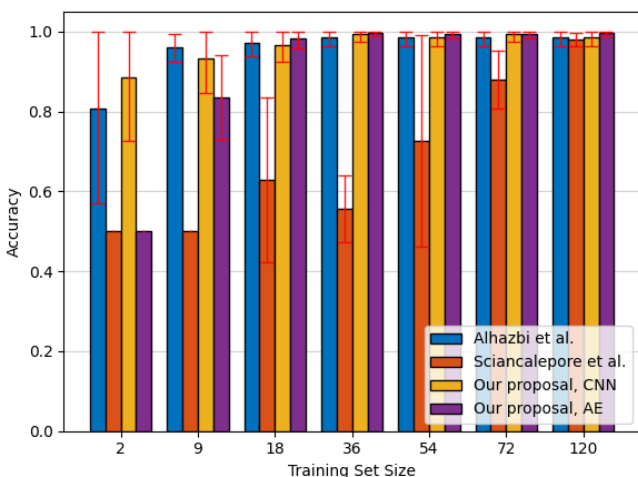


Figure 12: Accuracy as a function of the training set size. We compared our solutions with state-of-the-art contributions.

Jamming detection accuracy is positively correlated with the number of training images. However, using the approach

in [4] requires more images during the training phase to reach stable performance, i.e., 120 images, compared to the only 18 images required by our proposal. Jamming detection performances with our approach are very reliable when using 18 images, with both CNNs and AEs.

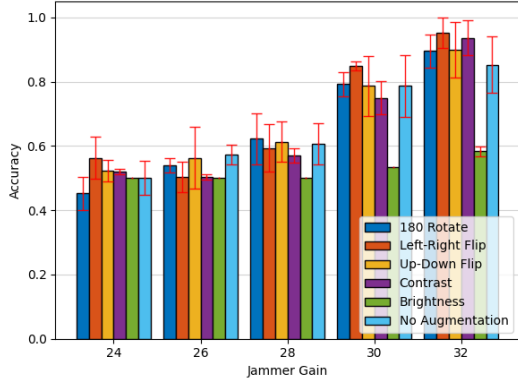
Exp. 3: Image Augmentation. We compare the accuracy of our proposed solutions with the literature, considering the adoption of various image augmentation techniques. For this test, we consider the data collected in the environment $E2$, as it provides a more challenging classification task, allowing us to test our solution in the worst-case scenario. We empirically select 150 images from the no-jamming dataset and 75 from the jamming dataset and investigate the effect of image augmentation against the benchmark proposals in [3] and [4] with $5 \cdot 10^4$ samples per image. We consider the following augmentation strategies, empirically chosen from those made available by Matlab [42]: (i) 180 degrees rotation, (ii) left-right mirror, (iii) up-down mirror, (iv) contrast increase and (v) brightness increase. We report all our results in Fig. 13. We report with the legend *No Augmentation* the performances obtained when only real-world data are used in the training set, providing a reference benchmark.

When using the AE-based one-class classification approach, as in Fig 13(a) and (c), the augmentation strategies *180 Rotate* (dark blue bar), *Left-Right Flip* (orange bar) and *Up-Down Flip* (yellow bar) perform similarly to each other and to using no augmentation, e.g., reporting an accuracy of 0.78 with a jammer gain value of 30 in Fig. 13(a). This indicates that the usage of such augmentation strategies does not decrease performances. The augmentation strategy *Brightness* (green bar) performs significantly worse, e.g., accuracy 0.5 with jammer gain value 30 in Fig. 13(a). *Contrast* works better for the benchmark approaches than ours, e.g., accuracy of 0.96 with jammer gain value 30 in Fig. 13(a). *Contrast* and *Brightness* perform the best for the CNN-based binary classification approach: CNN are exposed to both classes during training. The brightness of the image is correlated with the classification accuracy: bright clouds resemble no jamming, and dim clouds look like jamming. Therefore, using brightness as an augmentation parameter decreases the performance. Therefore, when choosing the right type of strategy, using augmentation during training does not decrease performance compared to using only real-world data (no augmentation). Thus, augmentation can be used as an effective strategy to increase the dataset when insufficient input data is available.

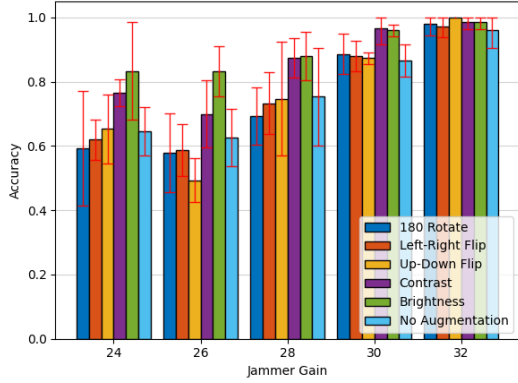
7.3. Jamming Parameters

In this subsection, we investigate the impact of various jamming parameters on the detection of weak jamming signals in the outdoor environment, including the jammer oversampling ratio, the jammer type, the jammer hardware, the jammer location, and the jammer distance from the communication link.

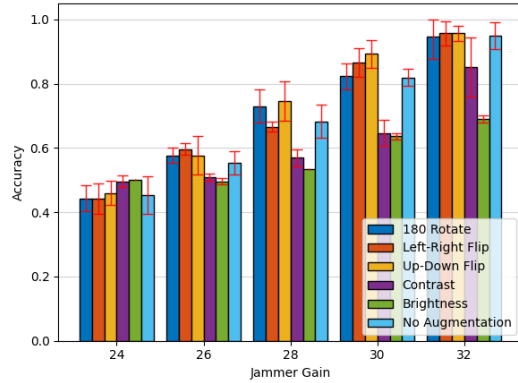
Exp. 4: Jammer Oversampling Ratio. We define *Jammer Oversampling Ratio* (JOR) as the ratio between the sample rate of the jammer and the sample rate of the legitimate communication link. Figure 14 reports the results of our analysis considering both the proposed jamming detection approaches in



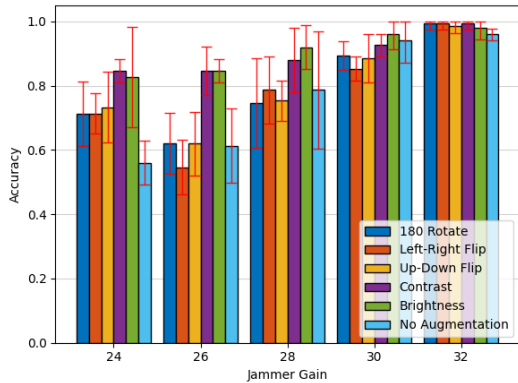
(a) Sciancalepore et al., [4]



(b) Alhazbi et al., [3]



(c) Our proposal, AEs



(d) Our proposal, CNN

Figure 13: Accuracy using various image augmentation techniques while considering $5 \cdot 10^4$ samples per image.

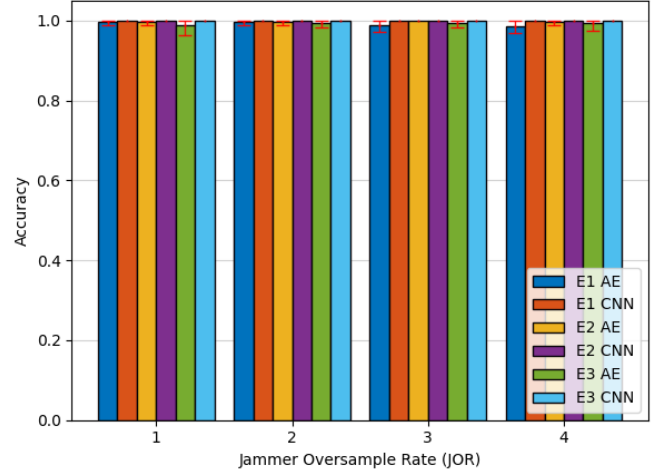


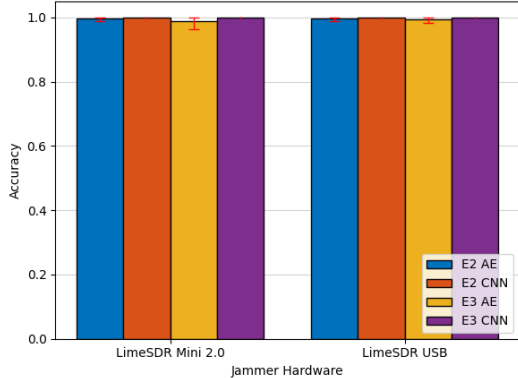
Figure 14: Classification accuracy varying the Jamming Oversampling Ratio (JOR) in environments $E1$, $E2$ and $E3$. JOR does not affect the performance of jamming detection.

the three measurement scenarios. The accuracy is near 1.0 for all environments and both detection approaches, demonstrating that increasing the sample rate is not a viable option for the jammer to avoid detection.

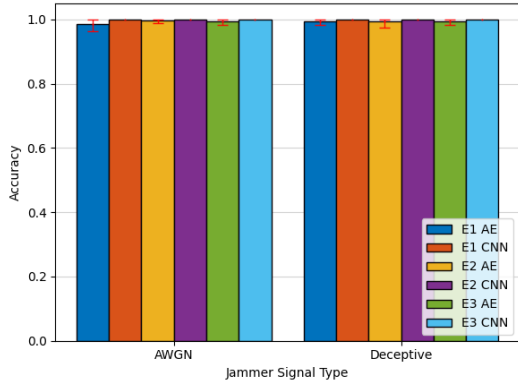
Exps. 5-7: Jammer Hardware, Location, and Type. We report in Figs. 15(a) and (b) the results of experiments investigating the impact of the *Jammer Hardware* and the *Jammer Signal Type*. Our results show that the considered hardware (LimeSDR Mini or LimeSDR) and the different jamming signals (AWGN or deceptive) do not affect the accuracy of our proposed techniques.

For the experiments on jammer location, we report in Fig. 16(a) the schematic of the layout used for the experiments. Figure 16(b) shows the results associated with the detection accuracy, confirming the robustness of our proposed solution in any relevant real-world environment.

Exp. 8: Jammer distance. We evaluate the impact of the distance of the jammer from the communication link on jamming detection accuracy. Figure 17 and 18 show the results for the jamming detection accuracy of the AE and CNN-based approaches at various distances for scenarios $E1$ and $E2$, respectively. All the proposed solutions have comparable performance in the environment $E1$; indeed, the accuracy is 1 for all the distances up to 23 m, where all the detection techniques have a drop in performance. In fact, 23 m is the distance where the signal power under jamming becomes comparable to the power of the legitimate signal at the receiver, i.e., $SNR_{DR} \approx 1$. In scenario $E2$, we observe a worse performance for the AE (E2 - Sciancalepore et al. [4] and E2 - Our proposal, AE). AE-based detection techniques are less prone to discriminate between interference and jamming, and we note that state-of-the-art solutions are more sensitive to this problem than ours. In general, the accuracy of our solutions is affected by the distance, starting at 23 meters in both outdoor environments. In fact, at such distances, the jamming signal is comparable to the legitimate one ($SNR_{DR} = 0.96$), making it difficult to detect.



(a) Jammer hardware



(b) Jamming signal

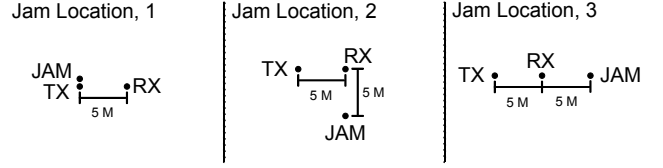
Figure 15: Performance of jamming detection as a function of the (jammer) hardware and (jamming) signal type.

7.4. Communication Parameters

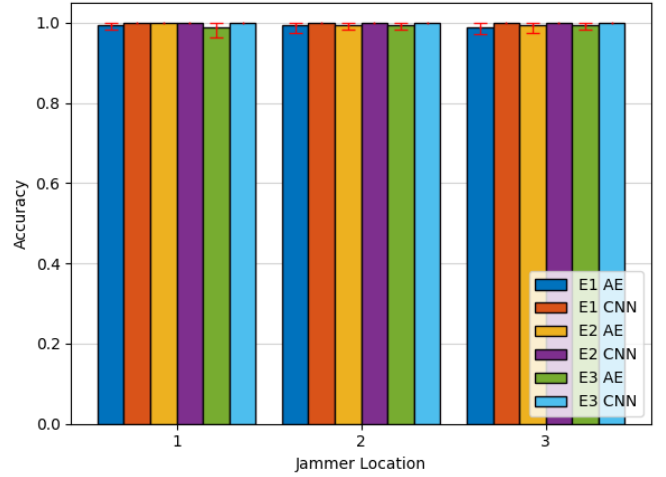
In this subsection, we investigate the performance of jamming detection considering various communication parameters, i.e., the modulation scheme used by the legitimate communication link, the SNR, the receiver distance from the jammer, and the mobility patterns of the receiver.

Exp. 9: Modulation Scheme. We consider different modulation schemes for the legitimate communication link among the supported options in IEEE 802.11g, i.e., BPSK, QPSK, 16-QAM and 64-QAM. We consider the setup shown earlier in Fig. 10, with the TX, RX, and Jammer gain values set to 66, 50, and 16, respectively. Note that we chose the setup and gain values such that the BER for the modulation 64-QAM—the most complex modulation scheme with the least margin for error—is as low as possible. To adapt the image generation method proposed in the literature to higher-order modulation schemes, we change the x-axis and y-axis limits to center the created clouds while keeping the same rationale. For BPSK, we use $[0, 2]$ and $[-1, 1]$; for QPSK, we use $[-0.293, 1.707]$ and $[-1, 1]$; for 16-QAM, we use $[-0.867, 2.133]$ and $[-1.5, 1.5]$, and finally, for 64-QAM, we use $[-0.883, 2.117]$ and $[-1.5, 1.5]$. Figure 19 shows the results of our experiments, considering both jamming detection approaches and the reference solutions in [3] and [4], in the environment $E2$.

The accuracy is consistent independently of the modula-



(a) Measurement setup



(b) Detection performance

Figure 16: Detection performance as a function of the relative positions of the jammer and the transmitter-receiver link.

tion scheme and the adopted detection technique. We notice a decrease in the accuracy for QPSK when using the AE-based approaches. This drop occurs because the selected (discrimination) threshold is too high, leading to some misclassifications. The CNN-based approaches can mitigate such limitations through the apriori knowledge of samples acquired on a jammed communication channel during training, showing their potential for enhanced jamming detection when applicable.

Exp. 10: Low Signal to Noise Ratio (SNR) Scenarios. We also investigate the impact of SNR on jamming detection. Since we cannot directly control the SNR on a real-world wireless channel, we indirectly influenced it using the gain value set at the transmitter. We use the setup shown earlier in Fig. 10, with gain values of 50 and 14 for the receiver and jammer, respectively. Due to the difference in signal propagation, we use different transmitter gains per environment: $[50, 55, 60, 65]$ for $E2$ and $[44, 49, 54, 59]$ for $E3$. We selected the lower SNR values such that the BER under jamming is less than 1% higher than the BER without jamming. We present the results for $E2$ in Fig. 20(a) and the results for $E3$ in Fig. 20(b).

Low SNR values do not significantly affect detection accuracy in an outdoor environment, as shown in Fig. 20(a)—these findings are in line with those of [43]. Slow fading, i.e., attenuation of the signal over long distances, also does not affect jamming detection accuracy. Fast fading, i.e., the variability of the noise affecting the RSS at a given distance, causes

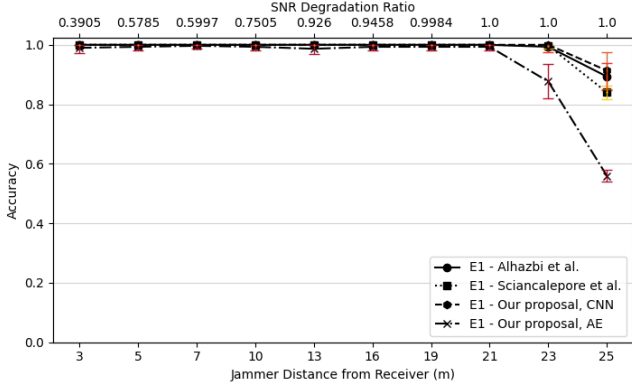


Figure 17: Classification accuracy varying the *Jammer Distance* in environment *E1*.

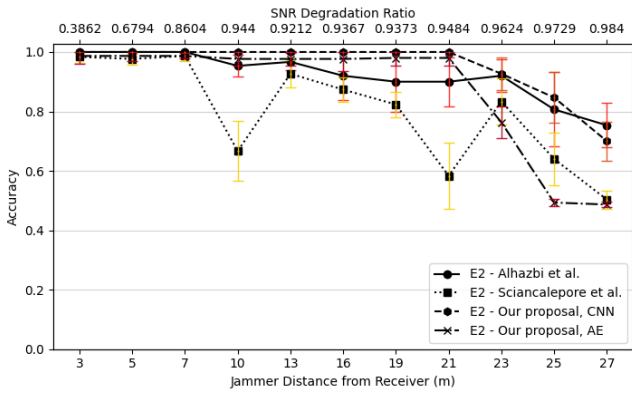


Figure 18: Classification accuracy varying the *Jammer Distance* in environment *E2*.

a more significant variance for RSS at more considerable distances. Therefore, the detection of jamming is not bound by the low SNR of the benign scenario. In contrast, the indoor environment (*E3*) affects the detection accuracy. As shown in Fig. 20(b), all detection approaches have a low detection accuracy for low SNR values. Thus, we can conclude that the jammer signal affects outdoor communications in a less destructive way due to the reduced multipath fading.

Exp.11: Receiver Distance. To analyze the importance of the SNR of the legitimate communication link for weak-jamming detection, we investigate the impact of the receiver distance from the transmitter on jamming detection accuracy. We present the results in Fig. 21 (environment *E1*) and Fig. 22 (environment *E2*). Jamming detection accuracy decreases as the effect of the jammer on the communication channel decreases due to the increased distance between the jammer and receiver. For scenario *E2*, the transmitter and receiver tests with a distance greater than 21 meters were not possible due to the reliability of the communication link at these distances. We experienced significant fluctuations in SNR, most likely due to multipath propagation.

Exp.12: Receiver mobility. Finally, we experiment with different mobility patterns, investigating jamming detection accuracy while the receiver moves. For this experiment, we used

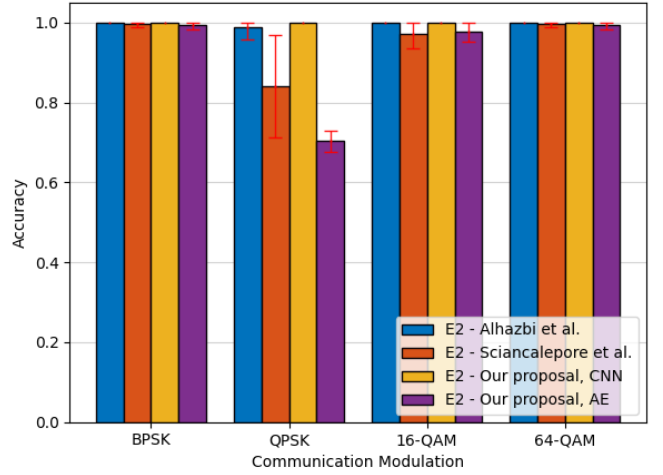


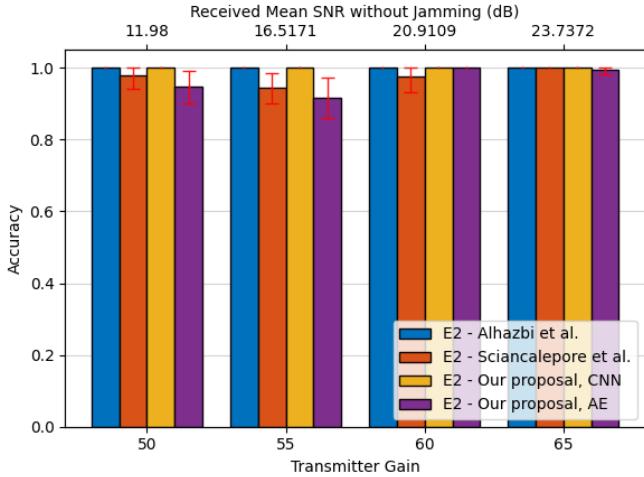
Figure 19: Classification accuracy for the AE and CNN-based approaches varying the *Communication Modulation Scheme* in environment *E2*.

the gain values 62, 50, and 44 for TX, RX, and jammer, respectively. The physical setup used for these experiments is depicted in Fig. 23(a) while Fig. 23(b) shows the three different mobility patterns considered: static, parallel, and perpendicular, respectively. The user moves up and down a 3-meter-long guide rail with a speed of approximately 12 meters per minute (2 times up and down every minute), bounded by our ability to keep it moving at a constant pace. The receiver is moved by pulling thin ropes attached to both ends of the receiver. Figure 24 shows the results of our tests for the three considered movement patterns.

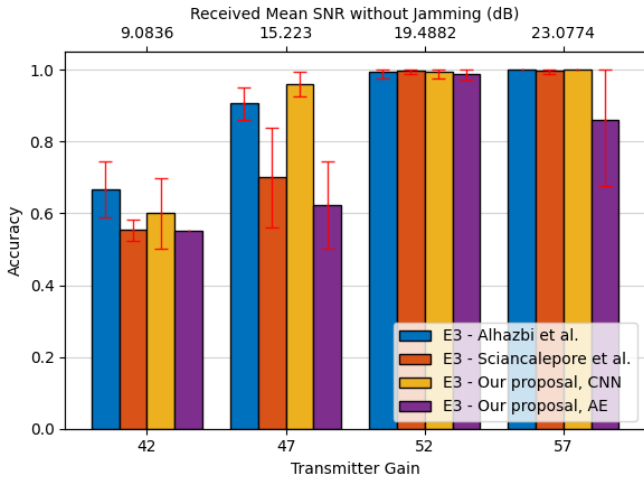
We observe a slight drop in performance (accuracy) for setup #3, i.e., the perpendicular movement of the receiver to the transmitter. This 10% drop, primarily relevant for the autoencoder using our solution for image generation, is likely due to the jammer having little effect on the communication link and becoming hardly detectable. Overall, our results confirm that receiver mobility does not affect the accuracy of jamming detection with any of the considered approaches.

7.5. Overhead evaluation

Finally, we consider the overhead introduced by our solution in terms of delay (processing time) and memory footprint. As previously discussed, our solution has been implemented in MatLab 2023a and run on an AMD Ryzen 9 5900 12-Core Processor, 3.00 GHz, 128GB RAM. Table 5 shows the breakdown of the overhead components in terms of time to generate an image (τ_{img}), time to test an image considering either the CNN-ResNet18 (τ_{cnn}) or the AE (τ_{ae}), respectively, the memory footprint for the CNN and AE models, i.e., M_{cnn} and M_{ae} , respectively, and finally, the memory footprint associated with an image, as a function of the number of samples per image. Overall, given the reference system considered in this work, the computation overhead sums up to (less than) 130ms and 28ms when considering CNN or Autoencoders, respectively, and the maximum number of samples per image (worst case), i.e., 10^5 The



(a) Scenario E2



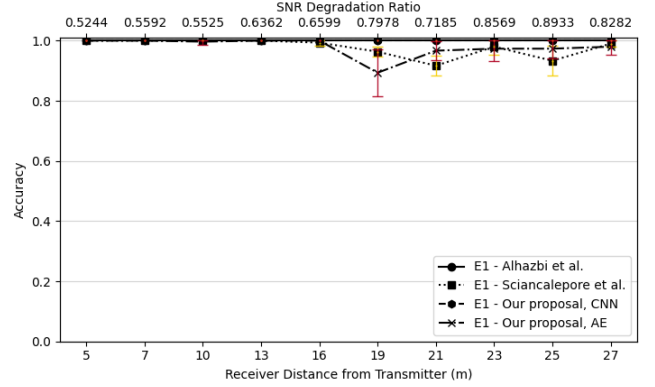
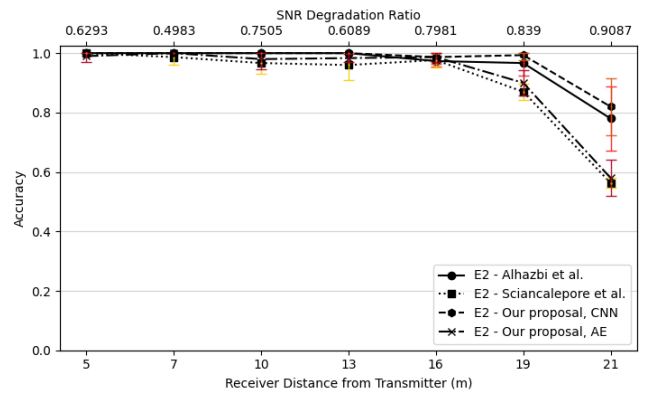
(b) Scenario E3

Figure 20: Classification accuracy varying the *Transmitter Gain*.

Samples per Image	10^4	$5 \cdot 10^4$	10^5
τ_{img} (ms)	10	10	20
τ_{cm} (ms)	13	55	110
τ_{ae} (ms)	3	5	8
M_{cm} (MB)	45	45	45
M_{ae} (MB)	14	14	14
M_{image} (KB)	151KB	151KB	151KB

Table 5: Overhead components of our solution.

memory footprint is independent of the number of samples per image but only depends on the type of neural network considered. We also observe that the image pre-processing technique has a negligible impact on the overall memory footprint since the generated images are very small (compared to the memory required by the model). The major overhead comes from the memory requirement to store the model, i.e., 14MB and 45MB for the Autoencoder and CNN, respectively. Conversely, the memory requirements for the image pre-processing are negligible and sum up to 151KB. Finally, we observe that the number of samples per image affects the processing time, and in par-

Figure 21: Classification accuracy varying the *receiver distance* in environment *E1*.Figure 22: Classification accuracy varying the *receiver distance* in environment *E2*.

ticular, CNNs perform much worse than autoencoders (they are more than 4 times slower, also due to running binary classification rather than one-class classification).

8. Discussion

Jamming Detection Approaches. Our results demonstrate that both AEs and the chosen CNN (Resnet-18) are reliable for weak-jamming detection. The two approaches exhibit similar performance when considering most jamming and communication parameters. However, the AE-based technique only requires *not-jammed samples* for the training process, i.e., the samples acquired during regular communications, which are easier to collect in practice. The CNN-based approach exhibits better performance when considering some image generation parameters (samples per image and training set size) and some *boundary conditions*, e.g., when the RSS of the legitimate communication link becomes comparable to the one of the jammer at the receiver side. However, being a binary classification approach, it requires training on samples from both classes (jammed and not-jammed IQ samples), which could be challenging to collect in many real-world scenarios. Our experiments considered several measurement parameters potentially impacting jamming detection. Many of such parameters are

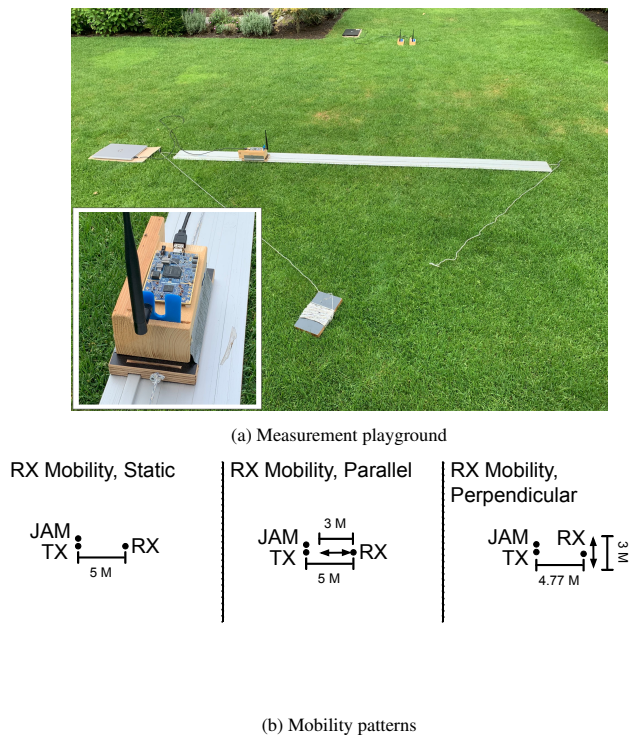


Figure 23: (a) Setup used for receiver mobility patterns and (b) movement patterns used for the experiments on the impact of receiver mobility on jamming detection. Two tent pegs at both ends of the guide rail allow us to move the receiver across the guide rail using two ropes. The close-up (bottom left) shows the cutout made in the wood to be compatible with the rail.

independent, but some of them are correlated: the jammer distance, transmitter gain, and receiver distance are all correlated through the SNR at the receiver. By comparing the results for these experiments among them, it is clear that the SNR is the (direct or indirect) variable mostly affecting the capability of detecting weak-jamming: when the SNR degrades significantly or is too low, all investigated jamming detection approaches struggle to detect jamming, while performances improve with lower SNR degradation ratios or higher absolute SNR values.

Comparison across Measurement Environments. The primary aim of this research is to compare various jamming detection methods in specific environments. In general, each environment is characterized by different propagation conditions, which require different fine-tuning of the transmission power and jammer power necessary to achieve weak jamming. In turn, such different configurations make systematic comparison among environments hard to achieve in a fair way across all experiments. However, as a by-product, our extensive experimental analysis also allows limited comparison of particular methods across scenarios. For example, the results for Experiment 4 (Jammer Oversampling Ratio), Experiment 6 (Jammer Signal Type) and Experiment 7 (Jammer Location) demonstrate that jamming detection across various Jamming Oversampling Ratio (JOR) values, jammer hardware and type is always possible independently of environment type. We also notice that multipath makes jamming detection harder, especially in low-SNR conditions. This is evident by comparing Fig. 17 with

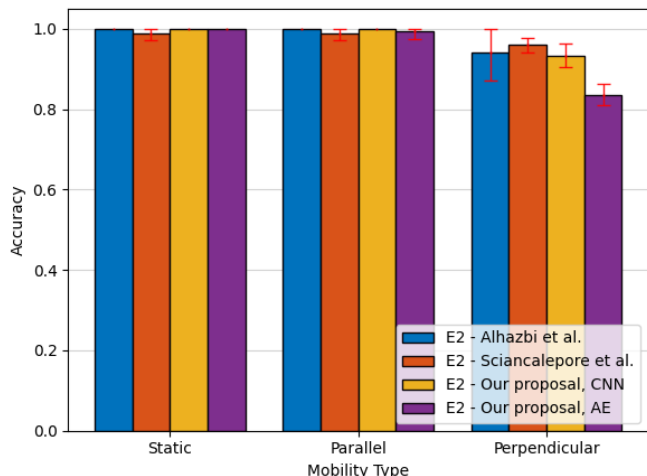


Figure 24: Classification accuracy with various receiver movement patterns in the environment $E2$.

Fig. 18 and Fig. 20 (a) with Fig. 20 (b): for both experiments, the presence of multipath leads to more unstable performances, indicating that multipath plays a role in making jamming detection more challenging. Future work could take these results as a starting point to execute a more systematic comparison of performances across measurement environments.

Image generation. When considering image generation techniques, state-of-the-art solutions from [3] and [4] exhibit some notable drawbacks. When using AEs, as proposed in [4], jamming detection requires more images in the training phase to be reliable (120 images vs. 9 of our proposal, Fig. 12). In addition, the solution in [4] is less resilient to interference (see Fig. 18). Although our solution performs slightly worse for some configurations (e.g., Fig. 24), overall, it performs more consistently than previous proposals and is compatible by design with any digital modulation scheme.

Limited Acquisition Bandwidth. For our experiments, the use of the LimeSDR USB forced us to use an acquisition bandwidth of 5 MHz instead of 20 MHz, as required by IEEE 802.11g. This reduced sample rate is a worst-case scenario for jamming detection at the PHY layer, since less information is available to the receiver for signal classification. Thus, using larger acquisition bandwidth does not affect our findings.

Limited Experiments Area. We acknowledge that the maximum distance considered for our experiments, i.e., 23 meters, may not be sufficiently representative of extensive jamming in large outdoor scenarios. This limitation of our study is mainly due to two factors. First, the outdoor areas available for our real-world experiments is limited, and we cannot legally perform extensive jamming outdoor without affecting the quality of WiFi services available to other users. Second, the equipment used for the experiments includes SDRs, which are not professional jammers capable of disrupting communications for hundreds of meters. Such devices have a limited transmission power and, in turn, they can jam nearby communications in a limited space. On the one hand, such a limitation motivates the need for additional work examining larger jamming distances,

which could enhance further the practical relevance and completeness of our study. On the other hand, we highlight that the maximum distance considered in our experiments (23 meters) is higher than the only contribution in the current literature investigating the impact of the jammer distance on the detection accuracy, i.e., the contribution in [4], which considered a maximum distance of 21 meters, only in an indoor environment. Moreover, although the existence of the limitations mentioned above, we remark that such limitations do not affect the validity of our findings and analysis. In fact, the aim of our analysis is to investigate the effectiveness of detecting weak jamming using various techniques proposed in the literature, and to find the boundary conditions where such techniques could detect weak jamming. As shown in Fig. 17 and Fig. 18, when the jammer is located 23 meters away from the receiver, all the investigated jamming detection approaches are characterized by sub-optimal performances, indicating that they cannot detect weak jamming reliably. As highlighted through the upper x-axis in those figures, these performances occur with a value of the SNR degradation ratio of 1.0 for the environment E1 (Fig. 17) and 0.984 for the environment E2 (Fig. 18). Similar considerations apply for Fig. 22. Therefore, the usage of more powerful devices over larger distances does not provide additional insight to our analysis and does not affect the validity of our conclusions.

Limited Training Data. For our analysis, we use up to 150 images of the *NO JAM* dataset for training and an equal number of *JAM* images, depending on the amount of jamming data available for the particular experiment. On the one hand, the usage of such a reduced number of images is an added value of our results. On the other hand, the number of images used for training is relatively limited. Thus, practitioners aiming to deploy our solution(s) in the wild should extend such a training dataset considering domain-specific datasets, collected directly in the environment where the solution is intended to be applied.

Jamming strategies. In our tests, in line with the relevant literature, we evaluated jamming detection considering AWGN and deceptive jamming. Our results are applicable independently from the number of frequencies targeted by the jamming, being it a spot jamming, sweep jamming, barrage jamming, or periodic jamming. However, the adversary could use more advanced types of jamming, e.g., reactive jamming. We first observe that continuous communication between the transmitter and the receiver translates reactive jamming into constant jamming, falling back into the analysis of this paper. When communication is not continuous, in line with the findings in [11], our solution is applicable when there are enough *JAM* samples part of an image to enable the correct image classification. The exact duration of the (reactive) jamming signal leading to detection always depends on the sample rate of the jammer and communication link and follows the results provided in Sec. 7.

Known Distance TX-RX. All the investigated approaches could require knowledge of the distance between the transmitter and receiver. Concerning the mobile scenario introduced in Sec. 4, mobile vehicles usually know such a distance from the communication link with the remote transmitter, e.g., through the adopted telemetry protocols. We recall that our solutions

detect jamming early, i.e., when the jamming on the receiver is weak and the communication link is still active. Thus, information availability is never a problem, contrary to *ex-post* approaches in the literature.

Scaling to Multi-channel and Multi-hop 802.11 Deployments. When considering extensive 802.11 deployments encompassing multiple channels and several hops separating IEEE 802.11 nodes, additional challenges apply. To name a few, neighboring 802.11 links could share partially overlapping channels, requiring extensive training to distinguish jamming from unintentional interference, even more with modulation schemes that admit interference by design (e.g., Non-Orthogonal Multiple Access — NOMA). Moreover, such complex networks require coordination mechanisms to detect and communicate jamming effects at scale. Thus, future research could investigate how to scale up this research to such scenarios.

9. Conclusion and Future Work

In this paper, we have presented an experimental evaluation of weak-jamming detection solutions, i.e., applying when the power of the jammer at the receiver is low, and the Bit-Error-Rate of the communication link is still not affected by the jammer. To this aim, we have extended our previous solutions to make them work reliably with an actual communication technology used by Commercial Off-The-Shelf devices, i.e., IEEE 802.11, and with the complex modulation schemes used in such a standard, i.e., OFDM with BPSK, QPSK, 16-QAM, and 64-QAM. We have also enhanced the state-of-the-art methodology for jamming detection through a new image generation approach, generalizing better to complex real-world modulation schemes. Thanks to an extensive experimental campaign using low-cost SDRs, we demonstrated the effectiveness of our enhanced solution in three heterogeneous wireless environments (indoor, outdoor with multipath, outdoor with minimal multipath) across an extensive range of jamming and communication parameters. As part of our future work, we plan to deploy our solution on real COTSs to evaluate the computational burden and energy overhead it incurs on such constrained devices. We will also investigate to what extent a sudden change in the movement type affect jamming detection capabilities.

References

- [1] H. Pirayesh and H. Zeng, “Jamming Attacks and Anti-Jamming Strategies in Wireless Networks: A Comprehensive Survey,” *IEEE communications surveys & tutorials*, vol. 24, no. 2, pp. 767–809, 2022.
- [2] X. Wang, J. Wang, Y. Xu, J. Chen, L. Jia, X. Liu, and Y. Yang, “Dynamic spectrum anti-jamming communications: Challenges and opportunities,” *IEEE Communications Magazine*, vol. 58, no. 2, pp. 79–85, 2020.
- [3] S. Alhazbi, S. Sciancalepore, and G. Oliveri, “Blood-Hound: Early Detection and Identification of Jamming at the PHY-layer,” in *IEEE Consumer Communications & Networking Conference (CCNC2023)*, 2023.

- [4] S. Sciancalepore, F. Kusters, N. K. Abdelhadi, and G. Oliveri, "Jamming Detection in Low-BER Mobile Indoor Scenarios via Deep Learning," *IEEE Internet of Things Journal*, vol. 11, no. 8, pp. 14 682–14 697, 2024.
- [5] M. Hanegraaf, S. Sciancalepore, G. Oliveri, "Open Source data of experiments for jamming detection," <https://tinyurl.com/4vvrammv>, <https://tinyurl.com/bwy88jrc>, 2024, (Accessed: 2025-Dec-15).
- [6] T. S. Rappaport, *Wireless Communications: Principles and Practice*. Cambridge University Press, 2024.
- [7] Y. Guo, Y. Liu, A. Oerlemans, S. Lao, S. Wu, and M. S. Lew, "Deep learning for visual understanding: A review," *Neurocomputing*, vol. 187, pp. 27–48, Apr. 2016.
- [8] D. Bank, N. Koenigstein, and R. Giryes, "Autoencoders," Apr. 2021, arXiv:2003.05991 [cs, stat].
- [9] Y. Feng, J. Chen, Z. Liu, H. Lv, and J. Wang, "Full Graph Autoencoder for One-Class Group Anomaly Detection of IIoT System," *IEEE Internet of Things Journal*, vol. 9, no. 21, pp. 21 886–21 898, 2022.
- [10] A. A. Cook, G. Mısırlı, and Z. Fan, "Anomaly Detection for IoT Time-Series Data: A Survey," *IEEE Internet of Things Journal*, vol. 7, no. 7, pp. 6481–6494, 2020.
- [11] G. Oliveri, S. Sciancalepore, S. Raponi, and R. Di Pietro, "PAST-AI: Physical-layer authentication of satellite transmitters via deep learning," *IEEE Transactions on Information Forensics and Security*, vol. 18, pp. 274–289, 2022.
- [12] G. Oliveri, S. Sciancalepore, and A. Sadighian, "SatPrint: Satellite Link Fingerprinting," in *Proceedings of the 39th ACM/SIGAPP Symposium on Applied Computing*, ser. SAC '24. New York, NY, USA: Association for Computing Machinery, 2024, p. 177–185. [Online]. Available: <https://doi.org/10.1145/3605098.3636011>
- [13] S. Alhazbi, S. Sciancalepore, and G. Oliveri, "The Day-After-Tomorrow: On the performance of radio fingerprinting over time," in *Proc. of the 39th Annual Computer Security Applications Conference*, 2023, pp. 439–450.
- [14] L. Papangelo, M. Pistilli, S. Sciancalepore, G. Oliveri, G. Piro, and G. Boggia, "Adversarial Machine Learning for Image-Based Radio Frequency Fingerprinting: Attacks and Defenses," *IEEE Communications Magazine*, pp. 1–7, 2024.
- [15] O. Puñal, I. Aktaş, C.-J. Schnelke, G. Abidin, K. Wehrle, and J. Gross, "Machine learning-based jamming detection for IEEE 802.11: Design and experimental evaluation," in *Proceeding of IEEE International Symposium on a World of Wireless, Mobile and Multimedia Networks 2014*, Jun. 2014, pp. 1–10.
- [16] Y. Li, J. Pawlak, J. Price, K. Al Shamaileh, Q. Niyaz, S. Paheding, and V. Devabhaktuni, "Jamming Detection and Classification in OFDM-Based UAVs via Feature- and Spectrogram-Tailored Machine Learning," *IEEE Access*, vol. 10, pp. 16 859–16 870, 2022.
- [17] A. Toma, A. Krayani, M. Farrukh, H. Qi, L. Marcenaro, Y. Gao, and C. S. Regazzoni, "AI-Based Abnormality Detection at the PHY-Layer of Cognitive Radio by Learning Generative Models," *IEEE Transactions on Cognitive Communications and Networking*, vol. 6, no. 1, pp. 21–34, Mar. 2020.
- [18] H. M. Furqan, M. A. Aygöl, M. Nazzal, and H. Arslan, "Primary user emulation and jamming attack detection in cognitive radio via sparse coding," *EURASIP Journal on Wireless Communications and Networking*, vol. 2020, no. 1, p. 141, Jul. 2020.
- [19] C. Zhang, L. Zhang, T. Mao, Z. Xiao, Z. Han, and X.-G. Xia, "Detection of Stealthy Jamming for UAV-Assisted Wireless Communications: An HMM-Based Method," *IEEE Transactions on Cognitive Communications and Networking*, vol. 9, no. 3, pp. 779–793, Jun. 2023.
- [20] Y. Arjoune, F. Salahdine, M. S. Islam, E. Ghribi, and N. Kaabouch, "A Novel Jamming Attacks Detection Approach Based on Machine Learning for Wireless Communication," in *2020 International Conference on Information Networking (ICOIN)*, Jan. 2020, pp. 459–464.
- [21] M. Spuhler, D. Giustiniano, V. Lenders, M. Wilhelm, and J. B. Schmitt, "Detection of Reactive Jamming in DSSS-based Wireless Communications," *IEEE Transactions on Wireless Communications*, vol. 13, no. 3, pp. 1593–1603, Mar. 2014.
- [22] S. Gecgel, C. Goztepe, and G. K. Kurt, "Jammer Detection based on Artificial Neural Networks: A Measurement Study," in *Proceedings of the ACM Workshop on Wireless Security and Machine Learning*, New York, NY, USA, May 2019, pp. 43–48.
- [23] A. Krayani, M. Baydoun, L. Marcenaro, Y. Gao, and C. S. Regazzoni, "Smart Jammer Detection for Self-Aware Cognitive UAV Radios," in *2020 IEEE 31st Annual International Symposium on Personal, Indoor and Mobile Radio Communications*, Aug. 2020, pp. 1–7.
- [24] B. Kihei, H. Wilson, and M. Fall, "Experimental Results of Detecting Primitive Jamming Attacks using Machine Learning in Vehicle-to-Everything Communication Networks," in *2021 IEEE 7th World Forum on Internet of Things (WF-IoT)*, Jun. 2021, pp. 530–535.
- [25] M. Bogdanoski, A. Risteski, P. Latkoski, and T. Shuminoski, "Power Control as an Effective Method against Low Power Jamming," in *Sixth International Conference on Computational Intelligence, Communication Systems and Networks*, 2014, pp. 101–106.

- [26] A. Garnaev, Y. Liu, and W. Trappe, "Anti-jamming Strategy Versus a Low-Power Jamming Attack When Intelligence of Adversary's Attack Type is Unknown," *IEEE Transactions on Signal and Information Processing over Networks*, vol. 2, no. 1, pp. 49–56, 2016.
- [27] N. Venkata Abhishek and M. Gurusamy, "JaDe: Low Power Jamming Detection Using Machine Learning in Vehicular Networks," *IEEE Wireless Communications Letters*, vol. 10, no. 10, pp. 2210–2214, 2021.
- [28] J. Villain, V. Deniau, C. Gransart, A. Fleury, and E. P. Simon, "Characterization of IEEE 802.11 Communications and Detection of Low-Power Jamming Attacks in Non-controlled Environment Based on a Clustering Study," *IEEE Systems Journal*, vol. 16, no. 1, pp. 683–692, 2022.
- [29] S. Saxena, A. Pandey, and S. Kumar, "RSS based multi-stage statistical method for attack detection and localization in IoT networks," *Pervasive and Mobile Computing*, vol. 85, p. 101648, 2022.
- [30] O. Savolainen, T. Malmivirta, Z. Yan, A. Morrison, and L. Ruotsalainen, "Towards Jammer Fingerprinting: The Effect of the Environment and the Receiver to a Jammer Classification," in *International Conference on Localization and GNSS (ICL-GNSS)*, 2024, pp. 1–7.
- [31] R. Chitaur, M. Brzozowski, O. Yener, and P. Langendörfer, "Real-Time Jamming Detection, Classification and Logging Using Computer Vision in 5G Private Networks," in *International Symposium on Wireless Communication Systems (ISWCS)*, 2024, pp. 1–6.
- [32] J. Smailes, E. Salkield, S. Köhler, S. Birnbach, M. Strohmeier, and I. Martinovic, "Sticky fingers: Resilience of satellite fingerprinting against jamming attacks," in *Workshop on Security of Space and Satellite Systems*, 2024.
- [33] Mathworks, "ResNet-18 convolutional neural network - MATLAB resnet18 - MathWorks Benelux," (Accessed: 2025-Dec-15). [Online]. Available: <https://nl.mathworks.com/help/deeplearning/ref/resnet18.html>
- [34] O. Russakovsky et al., "ImageNet Large Scale Visual Recognition Challenge," *Int. Jour. of Comp. Vision*, vol. 115, no. 3, pp. 211–252, 2015.
- [35] S. M. Erfani, S. Rajasegarar, S. Karunasekera, and C. Leckie, "High-dimensional and large-scale anomaly detection using a linear one-class SVM with deep learning," *Pattern Recognition*, vol. 58, pp. 121–134, Oct. 2016.
- [36] Lime Microsystems, "LimeSDR," (Accessed: 2025-Dec-15). [Online]. Available: <https://limemicro.com/products/boards/limesdr/>
- [37] G. Halfacree, "Lime Microsystems Unveils the LimeSDR Mini 2.0, with Larger and More Capable FPGA," Mar. 2022, (Accessed: 2025-Dec-15). [Online]. Available: <https://limemicro.com/news/lime-microsystems-unveils-the-limesdr-mini-2-0-with-larger-and->
- [38] GNURadio, "LinuxInstall - GNURadio," https://wiki.gnuradio.org/index.php/LinuxInstall#For_GNU_Radio_3.10,_3.9,_and_Main_Branch, (Accessed: 2025-Dec-15).
- [39] "Gr-limesdr Plugin for GNURadio - Myriad-RF Wiki," (Accessed: 2025-Dec-15). [Online]. Available: https://wiki.myriadrf.org/Gr-limesdr_Plugin_for_GNURadio#LimeSuite
- [40] "bastibl/gr-ieee802-11: IEEE 802.11 a/g/p Transceiver," (Accessed: 2025-Dec-15). [Online]. Available: <https://github.com/bastibl/gr-ieee802-11>
- [41] IEEE, "IEEE 802.11g-2003: Further Higher Data Rate Extension in the 2.4 GHz Band," Dec. 2003, (Accessed: 2025-Dec-15). [Online]. Available: <http://standards.ieee.org/getieee802/download/802.11g-2003.pdf>
- [42] "Get Started with Image Preprocessing and Augmentation for Deep Learning - MATLAB & Simulink - MathWorks Benelux," (Accessed: 2025-Dec-15). [Online]. Available: <https://nl.mathworks.com/help/images/get-started-with-image-preprocessing-and-augmentation-for-deep.html>
- [43] P. Tedeschi, S. Sciancalepore, and R. Di Pietro, "Modelling a Communication Channel under Jamming: Experimental Model and Applications," in *2021 IEEE Intl Conf on Parallel & Distributed Processing with Applications, Big Data & Cloud Computing, Sustainable Computing & Communications, Social Computing & Networking (ISPA/BDC/Cloud/SocialCom/SustainCom)*, Sep. 2021, pp. 1562–1573.